A time-lapse seismic repeatability test using the P-Cable high-resolution 3D marine acquisition system

Patrick Smith[1] and Brandon Mattox[2]

https://doi.org/10.1190/tle39070480.1

Abstract

The P-Cable high-resolution 3D marine acquisition system tows many short, closely separated streamers behind a small source. It can provide 3D seismic data of very high temporal and spatial resolution. Since the system is containerized and has small dimensions, it can be deployed at short notice and relatively low cost, making it attractive for time-lapse seismic reservoir monitoring. During acquisition of a 3D high-resolution survey in the Gulf of Mexico in 2014, a pair of sail lines were repeated to form a time-lapse seismic test. We processed these in 2019 to evaluate their geometric and seismic repeatability. Geometric repetition accuracy was excellent, with source repositioning errors below 10 m and bin-based receiver positioning errors below 6.25 m. Seismic data comparisons showed normalized root-mean-square difference values below 10% between 40 and 150 Hz. Refinements to the acquisition system since 2014 are expected to further improve repeatability of the low-frequency components. Residual energy on 4D difference seismic data was low, and timing stability was good. We conclude that the acquisition system is well suited to time-lapse seismic surveying in areas where the reservoir and time-lapse seismic signal can be adequately imaged by small-source, short-offset, low-fold data.

Introduction

Patented in 2003 (Planke and Berndt, 2003), the P-Cable high-resolution 3D marine acquisition system was commercialized in 2008. Its applications include near-surface stratigraphy investigations (Waage et al., 2018), geohazard analysis (Brookshire et al., 2016), shallow hydrocarbon exploration (Garden et al., 2017), and time-lapse seismic studies (Hatchell et al., 2017; Waage et al., 2019). The technology can provide 3D seismic data with higher temporal and spatial resolution than conventional marine streamer seismic surveying (Garden et al., 2017). Due to its small dimensions, it can operate safely in restricted areas. It is containerized so that vessels of opportunity can be used, enabling deployment at short notice and relatively low cost. These are attractive features for a time-lapse seismic reservoir monitoring system (Hatchell et al., 2019).

In 2014, NCS Subsea acquired a 3D P-Cable survey in the Gulf of Mexico. Toward the end of that survey, two nonadjacent sail lines were reacquired as a time-lapse seismic repeatability study. We reprocessed the data in 2019 to evaluate the method's suitability for reservoir monitoring. This paper describes the processing challenges encountered and documents the results that were achieved. We expect this to be of value to those considering the technology for time-lapse seismic surveying.

Data acquisition

The 2014 3D survey was acquired in the Gulf of Mexico, offshore Louisiana, approximately 240 km south of New Orleans as shown in Figure 1. The water depth in this area is approximately 700 to 900 m. Two nonadjacent sail lines (59977 and 60217) were reacquired to create two repeated pairs (sequences 347 to 349). The acquisition configuration is listed in Table 1, and the general layout is shown in Figure 2. The configuration provided four-fold common midpoint (CMP) coverage with 3.125 × 6.25 m bin spacing.

Navigation and geometric repetition accuracy

We evaluated the navigation data accuracy by detailed direct-arrival time picking for every recorded trace. Source-to-detector distances were generally accurate to less than 1 m. We found no evidence of significant navigation inaccuracy between lines, although our analysis was somewhat limited by the small data set.

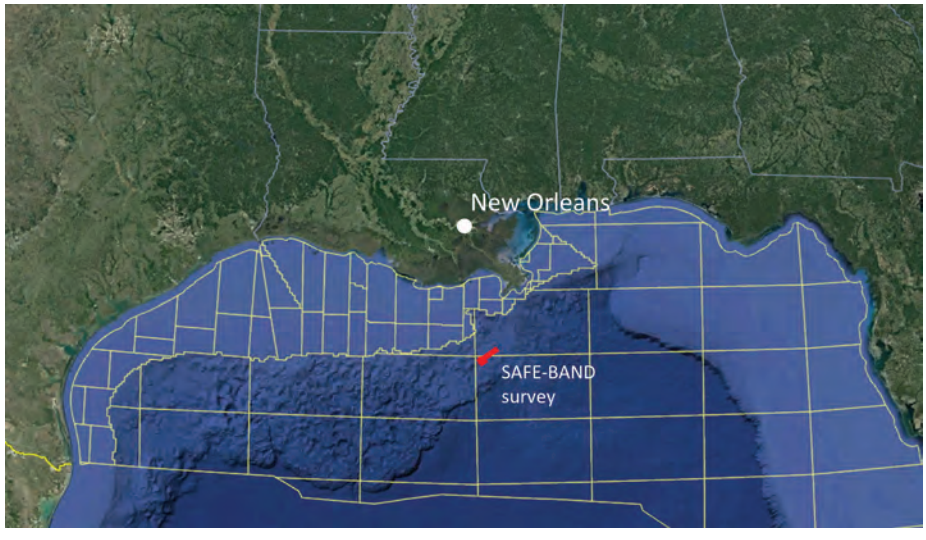

Figure 1. The location of the survey in the Gulf of Mexico, offshore Louisiana.

[1]WesternGeco, Stavanger, Norway. E-mail: psmith11@slb.com.
[2]NCS Subsea Inc., Stafford, Texas, USA. E-mail: brandon.mattox@ncs-subsea.com.

Table 1. The acquisition parameters of the repeatability test lines.

Streamer parameters			
Number of streamers	18	Streamer separation (m)	12.5
Number of groups per streamer	16	Group spacing (m)	6.25
Streamer depth (m)	2	Streamer type	GeoEel Solid
Source parameters			
Type	GI Harmonic	Number of guns	1
Array volume (in^3)	210	Pressure (psi)	2000
Depth (m)	3	Shot point interval (m)	12.5
Instruments			
Model	Geometrics CNT-2	Recording media	Hard Disk
Low-cut filter	N/A	High-cut filter	N/A
Record length(s)	4.25	Sample interval (ms)	0.25

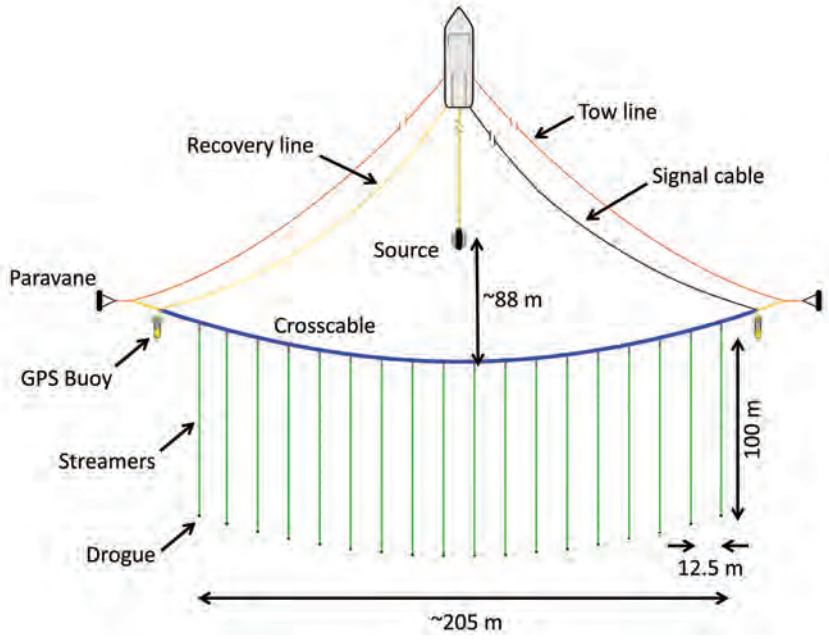

Figure 2. The general acquisition layout.

Accurate repetition of source and receiver locations is crucial for acquiring high-quality time-lapse seismic data (Calvert, 2005). Figure 3 shows histograms of the inline and crossline source repetition accuracy and crossline shot-by-shot receiver repetition accuracy. The source locations are generally repeated to within ±2 m in the inline direction, which compares well with conventional marine streamer acquisition. However, the acquisition system acquires shots at constant time intervals rather than at desired x, y coordinates. If vessel speeds differ significantly between lines, perhaps due to different current regimes, the inline repetition accuracy may be worse than encountered in this test. The crossline source repetition accuracy is generally better than 10 m, which again compares favorably with other acquisition methods.

The short cables mean that feathering has a minor impact, and so the receiver repetition accuracy for any given pair of colocated shots was generally better than 15 m. For a given CMP bin, the 12.5 m streamer separation gives a maximum positioning error of 6.25 m. However, crosscurrents do tend to move the entire spread in the crossline direction relative to the source, which may cause missing coverage when the source is steered along the preplot line. This could be alleviated by using overlap acquisition (e.g., using 18 streamers to acquire a 16-streamer preplot) or by dynamically steering the vessel in the crossline direction to optimize coverage (at the expense of a slight worsening of source repetition accuracy).

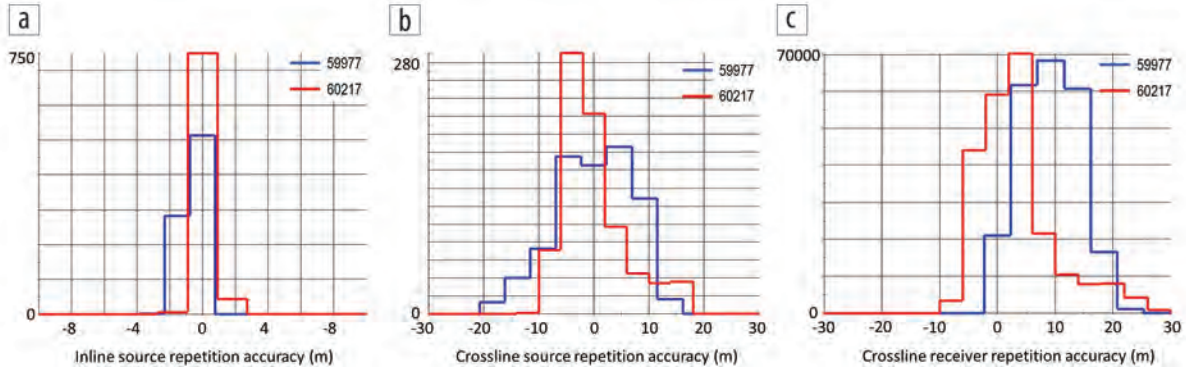

Figure 3. Histograms showing the (a) inline and (b) crossline source repetition accuracy and (c) crossline receiver repetition accuracy for colocated shots.

Seismic data quality

The recorded data were badly contaminated by streamer noise related to turbulence from the crosscable to which the streamers were attached. More modern versions of this acquisition system use noise-reduction fairings on the crosscable to reduce this. This survey relied on streamer ballasting and drogues at the end of the streamers for streamer depth control, which proved inadequate in the presence of strong loop currents. Analyzing the seismic data showed that the tail ends of the outer cables ran consistently deep (Figure 4), and the tail ends of all cables tended to vary in depth along each line. Frequently, the ends of the inner cables ran close to the surface, causing amplitude wipeouts and poor signal-to-noise ratio. The current version of the acquisition system avoids these issues by using depth controllers at the front and back of each cable.

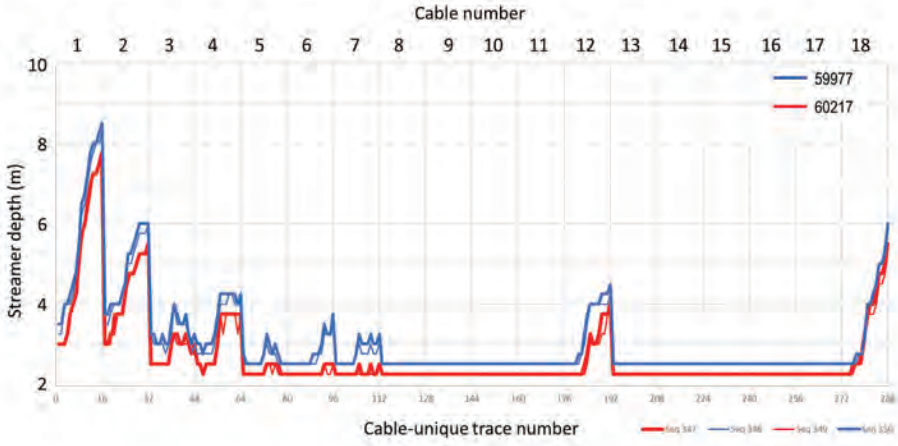

Figure 4. Line-averaged offset-variant cable depths estimated from seismic data for each of the four sequences acquired. The two members of each line pair are drawn with thick and thin lines. We believe that the consistency, in a line-averaged sense, of the estimated depths for cables 8–11 and 13–17 is genuine. However, accurate depth estimation can be challenging for shallow streamer depths.

Seismic data processing

We derived a comprehensive processing flow intended to address the data challenges and maximize time-lapse seismic repeatability. The flow includes the following steps:

1) Reformat from field data, timing delay correction, and navigation merge
2) Apply trace edit and low-cut filter
3) Perform swell-noise attenuation and despike
4) Estimate line-averaged streamer depths from seismic data
5) Compute and apply sail line-consistent trace-by-trace amplitude scalers from initially deghosted data
6) Derive and apply shot-by-shot time shifts to compensate sea-surface elevation changes at the source
7) Carry out incoherent noise attenuation
8) Execute additional swell-noise attenuation
9) Perform cable jerk noise removal
10) Resample from 0.25 to 1 ms sample interval
11) Apply 2D adaptive deghosting of source and receiver ghosts (Rickett et al., 2014) using the estimated depths as a starting point for the inversion
12) Derive and apply a second pass of sail line-consistent trace-by-trace amplitude scalers
13) Apply offset-variant CMP-by-CMP amplitude scalers to compensate for areas where the streamer tails ran shallow
14) Perform additional swell-noise attenuation with signal protection
15) Sort each sail line to four 3D cubes with 3.125 × 6.25 m cell size
16) Interpolate the 3D cubes to cell centers and constant offset, and select the center 10 inlines to generate 56.25 m wide 3D swaths of data
17) Two-dimensionally migrate each four-fold 3D inline independently using Kirchhoff prestack time migration and a supplied velocity field, combining the results to create a single 3D zero-offset cube
18) Apply 5 Hz low-cut filter
19) Execute 4D layer-parallel smoothing
20) Carry out local constrained cross equalization
21) Perform global match filtering
22) Apply time-variant band-pass filtering

We believed it was unnecessary to perform tide height corrections as we would be time aligning the sail-line pairs independently. However, it would be important to apply these corrections to a full-scale project. No designature was applied, as modeled signatures did not accurately represent the actual source bubble, and the data sets were too small to allow robust estimation of signatures from the data. The source bubble energy contaminated the sub-30 Hz frequency range, in which the signal-to-noise ratio was already poor, suggesting that compensating the bubble would provide little benefit. However, analysis of the final data sets suggests that debubble would have improved repeatability at lower frequencies, and future processing should include this. No demultiple was applied, as the water-layer multiples arrived quite deep in the recorded time range. A standard global 4D QC was performed after each major processing step to ensure that repeatability was improving.

Figure 5 shows octave band-pass filter panels for the near and far traces of cable 9 of sequence 348, computed close to the start of the processing flow. The signal-to-noise ratio is poor below approximately 30 Hz, particularly on the near traces, illustrating why the processing flow placed so much emphasis on noise attenuation. Also visible on the far traces are the bands of weak data, where the tail end of the streamer rose toward the surface. Figure 6 shows near- and far-trace amplitude spectra for a shot at the location of a band of weak data. The spectra are overlaid with the spectra of far-field signatures modeled with 2.5 m streamer depth on the near trace and 0.5 m streamer depth on the far trace. The data and modeled spectra match well. Note how the far-trace amplitude between 50 and 250 Hz is reduced by approximately

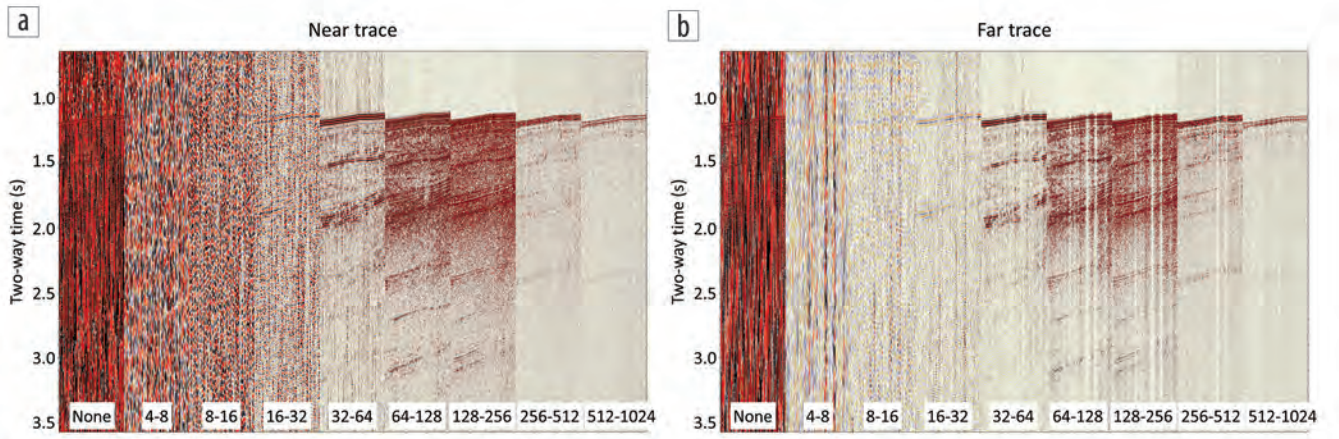

Figure 5. Octave band-pass filter panels for (a) near and (b) far traces from 150 contiguous shots of cable 9 of sequence 348.

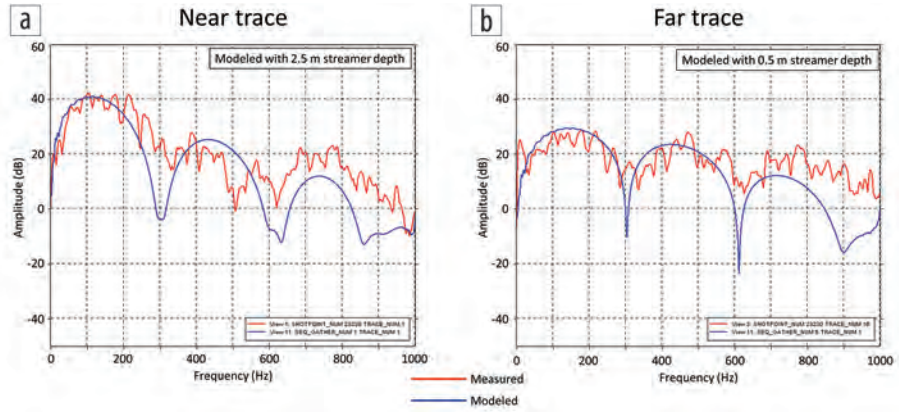

Figure 6. Amplitude spectra computed from (a) near- and (b) far-trace data (red) for a shot on sequence 347, where the tail end of the streamer runs shallow. Overlaid in blue are the spectra of far-field signatures modeled with source and receiver ghosts. The signature for the near trace was modeled with 2.5 m streamer depth, whereas 0.5 m was used for the far trace. A source depth of 2.5 m was used, based on the observed source ghost notch. The data spectra are computed in a 1000 ms window, starting 50 ms above the water bottom.

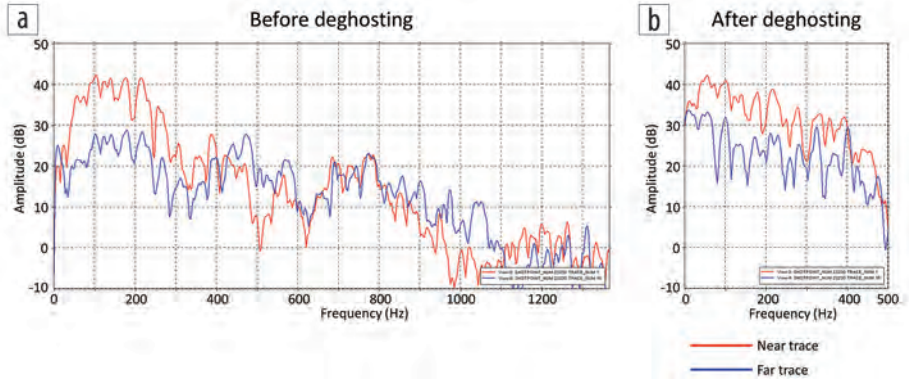

Figure 7. Amplitude spectra computed from the near- and far-trace data (red and blue, respectively) (a) before and (b) after deghosting for a shot on sequence 347, where the tail end of the streamer runs shallow. The spectra were computed in a 1000 ms window, starting 50 ms above the water bottom.

12 dB relative to the near trace, consistent with the observed weakness of the data. Note also the increase in low-frequency noise caused by the shallow tow depth. Figure 7 shows that deghosting compensates the source ghost and, on the near trace, the receiver ghost. It does not, however, manage to compensate the impact of the receiver ghost for the far trace. This is likely because the receiver ghost notch of this trace is beyond the Nyquist frequency associated with the 1 ms sample interval at which deghosting was applied. Even so, after deghosting, the amplitude difference between near and far trace over the main bandwidth of interest is roughly constant, supporting the simple amplitude scaling procedure that we used to correct the issue.

Figure 8 shows line-averaged near- and far-trace amplitude spectra for cable 1, where the tail end of the streamer runs consistently deep. The difference in the streamer ghost notches is clearly visible before deghosting, and we see that deghosting normalizes the near- and far-trace spectra nicely.

The extensive noise attenuation that we applied tended to reduce the temporal and spatial resolution relative to what is normally achieved with this acquisition system, but this is unlikely to be an issue for most time-lapse seismic applications. The noise-attenuation processes were parameterized to operate consistently between data sets, as would be done for a real time-lapse seismic project.

The shot-consistent time shift corrections were generally less than ±0.5 ms, which is consistent with the 1.5 m swell documented during acquisition. The corrections had a noticeable impact on repeatability at higher frequencies. The joint decomposition approach that was used ensures consistency between the data sets, but requires that no reservoir-related timing differences between surveys are present in the analysis window. This was not an issue for this data set, but real time-lapse seismic projects will require careful selection of analysis windows using

knowledge of the reservoir location and possible compaction-related changes in the overburden.

The success of the timing corrections left relatively little work for the local constrained cross equalization. Timing corrections were less than ±0.2 ms and amplitude corrections were generally less than ±0.5 dB. Similar comments apply to the choice of analysis windows.

Results

Figure 9 shows an inline through the final stack cube for sequence 348 (a member of the pair for line 59977) and the 4D difference data set (scaled by a factor of four relative to the stack). The residual energy around primary events on 4D difference data is quite low relative to that of the stacked data. Some of the residuals are related to using 2D migration — these would most likely be less obtrusive when better focused by 3D migration. Water-layer multiples are not very obvious on the 4D difference data. This is probably because the speed of sound in the water column did not change much in the

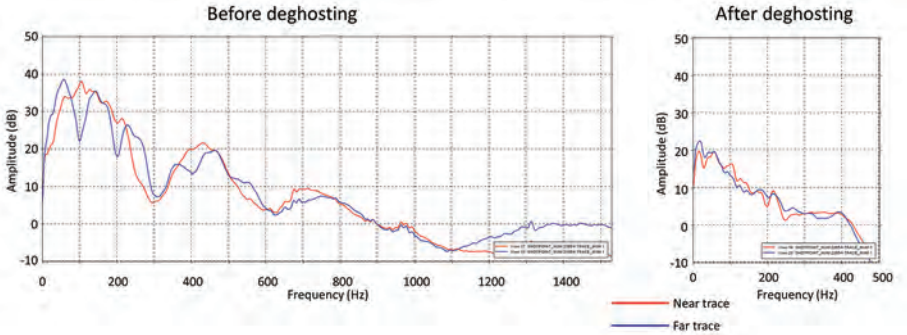

Figure 8. Line-averaged amplitude spectra computed from the near- and far-trace data (red and blue, respectively) of cable 1 of sequence 347. The far end of this cable runs consistently deep, as shown in Figure 4. The spectra were computed in a 1000 ms window, starting 50 ms above the water bottom.

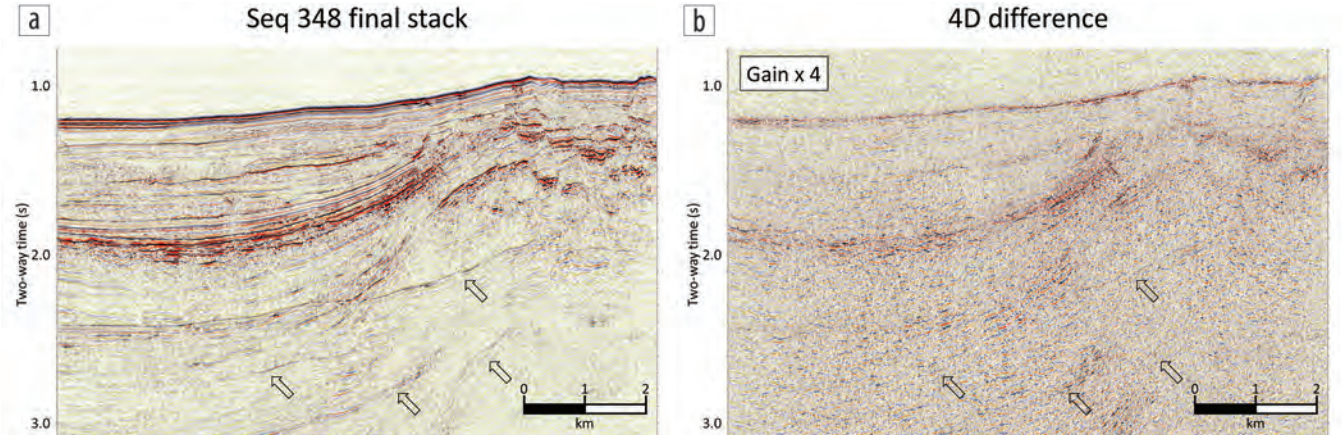

Figure 9. An inline from the final stack cube for (a) sequence 348 and (b) the 4D difference between sequences 348 and 350, gained by a factor of four relative to the stack. Water-layer multiples are highlighted with arrows.

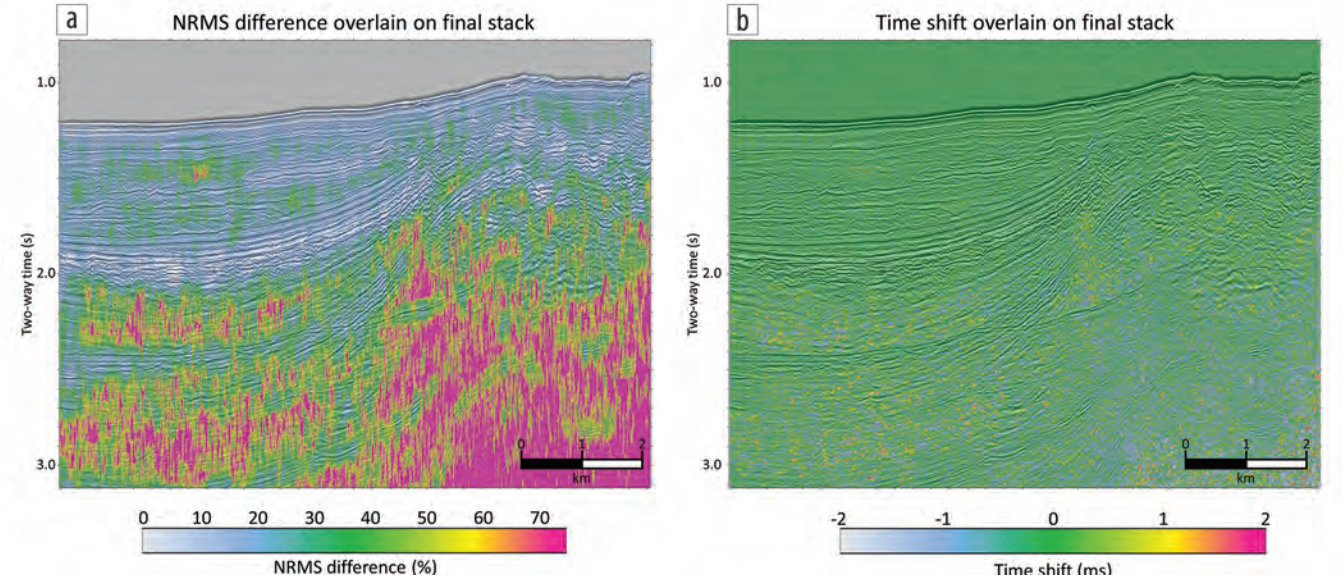

Figure 10. An inline from the final stack cube for sequence 348 overlaid with (a) NRMS difference and (b) time shift.

short time period between acquisition of the two lines. Figure 10a shows sample-by-sample normalized root-mean-square (NRMS) difference (Kragh and Christie, 2002) overlaid on the stacked data shown in Figure 9. The very low values of NRMS difference around the strongest events suggest that the data are well repeated, and that background noise is the main source of nonrepeatability.

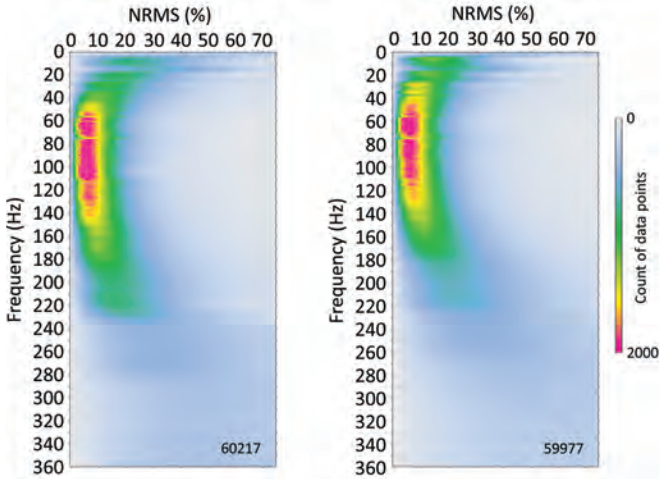

Figure 11. Frequency-variant NRMS difference histograms for the two data sets, computed in a 1000 ms window, starting 50 ms above the water bottom. Data from the entire 3D cube were included in each analysis.

Figure 10b shows sample-by-sample time shifts computed between the two members of the line pair. The timing is very stable down to approximately 2000 ms. The high NRMS levels and rather variable time shifts at depth are perhaps unsurprising, given the small source, small-offset range, and low fold of the data.

Figure 11 shows that the NRMS difference is generally well below 10% for frequencies between approximately 50 and 150 Hz. The repeatability becomes progressively worse above 150 Hz, even though Figure 5 suggests that the best signal-to-noise ratio is present between 130 and 250 Hz. It is probably unrealistic to expect a low NRMS difference at these very high frequencies, given the extreme acquisition and processing repeatability that would be required to achieve this.

We see NRMS values between 10% and 20% below approximately 30 Hz, whereas well-repeated deep-tow marine-streamer time-lapse seismic data sets typically exhibit NRMS values of 10% or less in this frequency band. The higher values on this data set are mainly due to poorer signal-to-noise ratio at these frequencies. There is some rapid variability in the NRMS trend at approximately 12 and 30 Hz that we suspect is related to the source bubble energy that the processing flow did not attenuate. Overall, the results are consistent with those presented by Hatchell et al. (2017).

Figure 12 shows 4D QC attribute maps for the final 3D cubes of line 60217, computed after band limiting from 0 to 40 Hz and from 40 to 140 Hz. The NRMS difference values are approximately

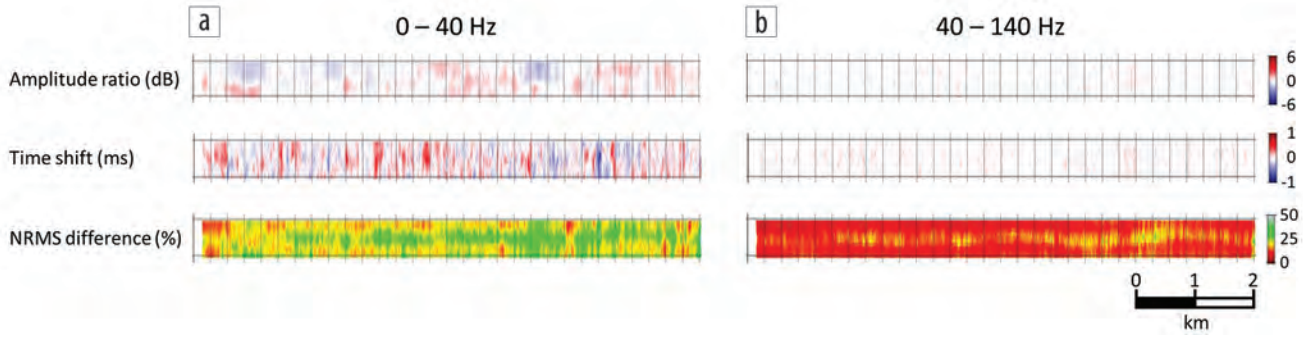

Figure 12. 4D QC attribute maps computed from the 3D stack cubes for line 60127 over (a) a 0 to 40 Hz frequency band and (b) a 40 to 140 Hz band. The analysis window was 1000 ms long and started 50 ms above the water bottom. The 3D cubes are 10.2 km long and 56.25 m wide.

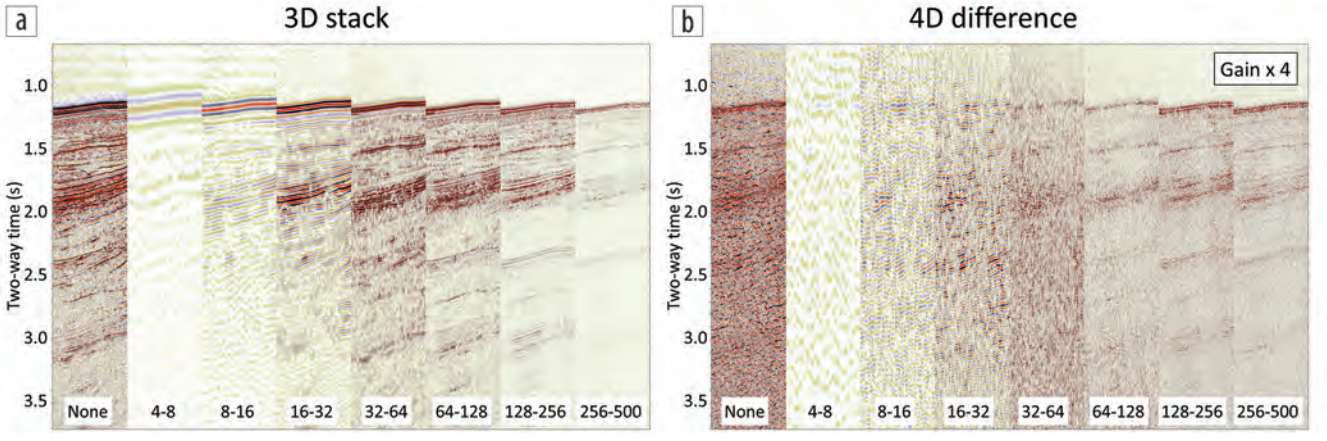

Figure 13. Octave filter panels on an inline from the (a) 3D stack cube for sequence 348 and (b) the equivalent 4D difference over the same area as shown in Figure 5. The 4D difference data are scaled by a factor of four relative to the stack.

12% in the 40 to 140 Hz band and greater than 20% in the lower-frequency band. The NRMS values are higher down the center of the swath, as this is the area in which the shallower streamers caused higher noise levels. The time shift and amplitude ratio values are close to zero in the 40 to 140 Hz band, largely because the 4D corrections were computed in this window and over a similar bandwidth. The attributes are more variable in the 0 to 40 Hz band, suggesting that intersurvey variability at lower frequencies has not been fully corrected. The time shifts vary by less than ±0.5 ms, which is insignificant in this frequency band, as evidenced by the lack of correlation between features on the time shift and NRMS difference maps. The amplitude ratio variations, although generally less than ±1 dB, do have some impact on the seismic repeatability in this band, as seen on the NRMS difference map and when visually inspecting the 4D difference seismic data. The variations correlate with areas where variable crosscurrents have moved one member of the pair relative to the other in the crossline direction, so that a given CMP bin compares data from different cables. This suggests that, while the processing flow has successfully normalized data for a given cable from one member of the sail-line pair to the next, it has not completely matched the impact of differing tow depths on data from different cables in this frequency band.

Figure 13 shows octave filter panels produced from the final stack for sequence 348 and the associated 4D difference (scaled by a factor of four). The seismic processing flow has clearly extracted signal from underneath the noise in the lower-frequency bands. But, we see evidence of instability (small segments of coherent high-amplitude residuals) in these bands, consistent with the observations from Figure 12. This would hamper identification of 4D signal in these frequency bands, depending on the magnitude and spatial coherency of the signal. The better streamer depth control expected from the upgraded acquisition system should alleviate these issues.

Discussion

Superficially, the 4D differences and 4D QC attributes from this test compare favorably with those expected from conventional marine streamer acquisition. But, there are some important differences.

In regions where the depth interval between the water bottom and reservoir is large, the usable frequency range at reservoir level tends to be limited by absorption of high-frequency energy in the overburden. In addition, high-frequency shot-generated off-line scattered noise and water-layer multiples of this scattered noise interfere with the signal at reservoir level. In some Norwegian Sea reservoirs, little usable energy above approximately 40 Hz is present. Even with the upgrades to the acquisition system, and perhaps by towing the source and streamers deeper than was done here, the signal-to-noise ratio in the 0–30 Hz band at depths of 2 km or more below water bottom is unlikely to match that of a deep-tow, long-offset, high-fold broadband marine streamer or ocean-bottom seismic survey. Feasibility studies should carefully evaluate the impact of absorption, noise, multiples, and any time-lapse signal tuning effects related to the potential lack of low-frequency content. The limited energy available from the small source should also be considered.

The short streamers preclude analysis of time-lapse amplitude changes with offset. This may be a significant issue for fields where the time-lapse reflectivity changes are most obvious at higher reflection angles. Time-lapse acoustic impedance inversion will probably need to make more use of low-frequency a-priori information than if more conventional acquisition techniques were used. Seismic data processing will generally rely on seismic velocities from preexisting data acquired with longer offset ranges.

Nevertheless, the technique seems well suited to time-lapse seismic reservoir monitoring in areas where the reservoir is shallow (less than 1 or 2 km) relative to the water bottom. Hatchell et al. (2019) show reservoir monitoring examples from the Gulf of Mexico, and similar opportunities most likely exist offshore West Africa and offshore Brazil. The method also has potential for monitoring shallow hazards and CO_2 storage.

Conclusions

P-Cable acquisition can provide high-quality time-lapse seismic information in areas where the reservoir can be adequately imaged by small-source, short-offset, low-fold data. Its relatively low cost, flexibility, and safety in restricted areas makes it an attractive option for frequent reservoir monitoring. Refinements to the hardware and operational procedures made since these tests were acquired are expected to further improve the results shown here. TLE

Acknowledgments

The authors thank NCS Subsea and WesternGeco for permission to present this paper. We also thank Nick Moldoveanu, Carlos Son, and Larry Scott for their support, and the reviewers for their constructive comments.

Data and materials availability

Data associated with this research are confidential and cannot be released.

Corresponding author: psmith11@slb.com

References

Brookshire, B. N., C. Lippus, A. Parish, B. Mattox, and A. Burks, 2016, Dense arrays of short streamers for ultrahigh-resolution 3D seismic imaging: The Leading Edge, **35**, no. 7, 594–599, https://doi.org/10.1190/tle35070594.1.

Calvert, R., 2005, Insights and methods for 4D reservoir monitoring and characterization: SEG and EAGE.

Garden, M., O. Michot, M. Terenzoni, H. H. Veire, J. R. Granli, L. M. Moskvil, and K. I. Krathus-Larsen, 2017, Resolution, resolution, resolution — An ultra-high resolution seismic case study from the Barents Sea: 79th Conference and Exhibition, EAGE, Extended Abstracts, https://doi.org/10.3997/2214-4609.201701138.

Hatchell, P., M. Rahimin Kamarudin, K. Wang, J. Lopez, S. Bakku, Z. Yang, A. Kudarova, et al., 2017, Low-cost, high-resolution 3D and 4D seismic for deepwater fields: 87th Annual International Meeting, SEG, Expanded Abstracts, 5782–5786, https://doi.org/10.1190/segam2017-17723832.1.

Hatchell, P., S. Bakku, and Z. Yang, 2019, 4D seismic of deep reservoirs with a low-cost P-Cable system: 81st Conference and Exhibition, EAGE, Extended Abstracts, https://doi.org/10.3997/2214-4609.201901589.

Kragh, E., and P. Christie, 2002, Seismic repeatability, normalized rms, and predictability: The Leading Edge, **21**, no. 7, 640–647, https://doi.org/10.1190/1.1497316.

Planke, S., and C. Berndt, 2003, Apparatus for seismic measurements: Norwegian Patent 317652 (U.K. Patent GB 2401684; U.S. Patent US 7,221,620 B2).

Rickett, J. E., D. J. van Manen, P. Loganathan, and N. Seymour, 2014, Slanted-streamer data-adaptive deghosting with local plane waves: 76th Conference and Exhibition, EAGE, Extended Abstracts, https://doi.org/10.3997/2214-4609.20141453.

Waage, M., S. Bünz, R. Bøe, and J. Mienert, 2018, High-resolution 3D seismic exhibits new insights into the middle-late Pleistocene stratigraphic evolution and sedimentary processes of the Bear Island trough mouth fan: Marine Geology, **403**, 139–149, https://doi.org/10.1016/j.margeo.2018.05.006.

Waage, M., S. Bünz, M. Landrø, A. Plaza-Faverola, and K. A. Waghorn, 2019, Repeatability of high-resolution 3D seismic data: Geophysics, **84**, no. 1, B75–B94, https://doi.org/10.1190/geo2018-0099.1.